Mechanobiologically optimized Ti–35Nb–2Ta–3Zr improves load transduction and enhances bone remodeling in tilted dental implant therapy

Chuanyuan Mao [a,1], Weijun Yu [a,1], Min Jin [a], Yingchen Wang [b], Xiaoqing Shang [c], Lu Lin [a], Xiaoqin Zeng [c,***], Liqiang Wang [b,**], Eryi Lu [a,*]

[a] *Department of Stomatology, Renji Hospital, School of Medicine, Shanghai Jiao Tong University, Shanghai, 200127, China*
[b] *State Key Laboratory of Metal Matrix Composites, School of Materials Science and Engineering, Materials Genome Initiative Centre, Shanghai Jiao Tong University, Shanghai, 200240, China*
[c] *National Engineering Research Center of Light Alloy Net Forming, School of Materials Science and Engineering, Shanghai Jiao Tong University, Shanghai, 200240, China*

ARTICLE INFO

ABSTRACT

The tilted implant with immediate function is increasingly used in clinical dental therapy for edentulous and partially edentulous patients with excessive bone resorption and the anatomic limitations in the alveolar ridge. However, peri-implant cervical bone loss can be caused by the stress shielding effect. Herein, inspired by the concept of "materiobiology", the mechanical characteristics of materials were considered along with bone biology for tilted implant design. In this study, a novel Ti–35Nb–2Ta–3Zr alloy (TNTZ) implant with low elastic modulus, high strength and favorable biocompatibility was developed. Then the human alveolar bone environment was mimicked in goat and finite element (FE) models to investigate the mechanical property and the related peri-implant bone remodeling of TNTZ compared to commonly used Ti–6Al–4V (TC4) in tilted implantation under loading condition. Next, a layer-by-layer quantitative correlation of the FE and X-ray Microscopy (XRM) analysis suggested that the TNTZ implant present better mechanobiological characteristics including improved load transduction and increased bone area in the tilted implantation model compared to TC4 implant, especially in the upper 1/3 region of peri-implant bone that is "lower stress". Finally, combining the static and dynamic parameters of bone, it was further verified that TNTZ enhanced bone remodeling in "lower stress" upper 1/3 region. This study demonstrates that TNTZ is a mechanobiological optimized tilted implant material that enhances load transduction and bone remodeling.

1. Introduction

Implant therapy is a well-established dental treatment modality that provides benefits for edentulous and partially edentulous patients [1]. But when faced with excessive bone resorption caused by some physiologic or pathologic factors and the anatomic limitations (such as mandibular canal and maxillary sinus) of the residual bone, a large proportion of these patients usually are unable to use the straight insertion of the dental implants because of the insufficient height of the alveolar ridge [2]. Recently, through an alternative strategy introduced by Maló et al. [3], implants can be placed inclined for edentulous and partially edentulous patients. This method of tilted implant with immediate function is increasingly used in clinical dental treatment [4]. However, the latest consensus statement and research suggested that tilting the implant may affect peri-implant bone response [5,6]. Also, the peri-implant bone loss around the cervical region could be caused by stress shielding effect [7,8]. Besides, there were limited studies about the combination with mechanical characteristics of implant material

and the *in vivo* biological features of bone for tilted implantation [9].

According to Wolff's law, the mechanical stress around bone tissue plays a crucial role in bone quality and architecture since stress is an essential stimulus in the natural process of bone healing and remodeling. However, Ti–6Al–4V (TC4) as one of the commonly used implant materials in the clinic has much higher elastic modulus (110 GPa) than human bone (0.69–30 GPa) [10,11]. This significant large mismatch between the elastic modulus of a load-bearing implant and that of the bone impedes the stress transfer from the implant to the bone and within the bone [12]. Moreover, the biomechanically induced failures could be explained as the major reason leading to the implant losses, and as an important factor affecting peri-implant bone density [13].

Recent studies suggested that novel implant metals are needed for better mechanotransduction, came up with solutions in reduction of implant metal elastic modulus or introduction of pores to metals, but hard to achieve mechanical properties of elastic modulus and strength for the clinical need at the same time [14,15]. One of the promising approaches to solve these issues is the application of plastic deformation to simultaneously attain enhanced strength and ductility performance along with low elastic modulus [16]. The deformation processing conditions, including deformation states and strain parameters, play a substantial role in the modification of mechanical properties in metallic

materials [7,17]. Ti–35Nb–2Ta–3Zr (TNTZ) is a newly developed β-type titanium (Ti) alloy for biomedical applications, containing only non-toxic elements and exhibiting excellent biocompatibility and bio-corrosion resistance. In our previous study, plastic deformation methods were employed to refine the microstructure of TNTZ and had achieved a better balance between elastic modulus and strength. We also showed that the deformation products of TNTZ that are generated during plastic deformation may change its elastic modulus [18]. TNTZ alloy has reached good elastic properties (Young's Modulus <60 GPa, elastic limit 340 MPa [19], Poisson's ratio 0.3–0.4 [20,21]) in previous studies. Based on previous work, in this study, the deformation processing conditions were further modulated in hot rolling to achieve controllable elastic modulus as well as strength in TNTZ.

To systematically validate these materiobiological questions, a serial of hot rolling methods was employed for producing a novel TNTZ implant with elastic modulus similar to bone and high strength. Subsequently, the influence of preparation process was elucidated on TNTZ's mechanical properties, and *in vitro* studies were designed to investigate the cell biocompatibility of TNTZ. It was hypothesized that a design of TNTZ with a similar elastic modulus to the bone would provide a beneficial mechanical environment for peri-implant bone remodeling in tilted implantation. To investigate the peri-implant bone stress
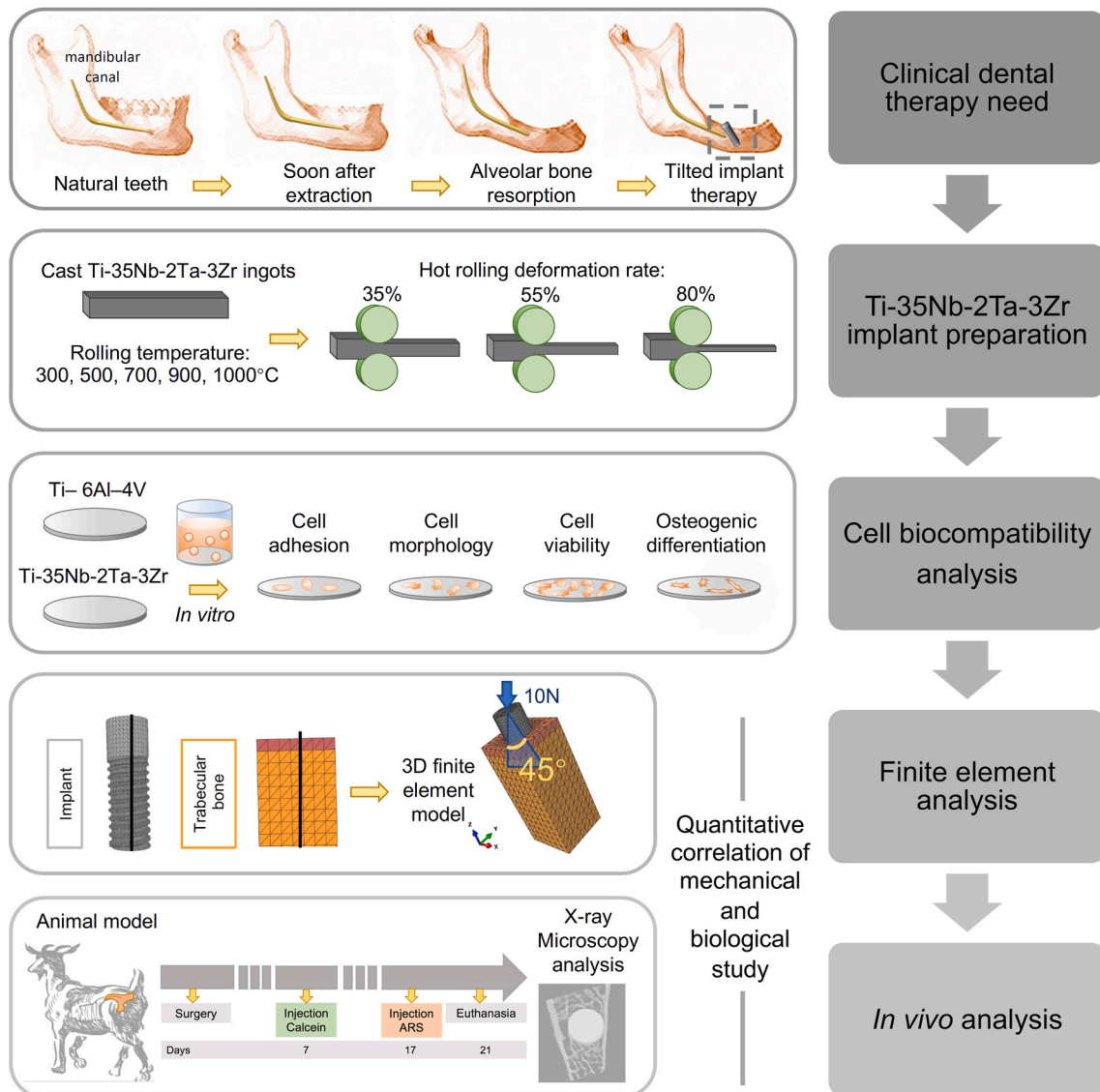

Fig. 1. Experimental schematic diagram.

distribution and related bone response, TNTZ and TC4 tilted implants under immediate loading in alveolar bone condition were mimicked in finite element (FE) and *in vivo* models, meanwhile, a layer-by-layer quantitative correlation of FE and X-ray Microscopy (XRM) analysis were conducted. Finally, this study focused on the "lower stress" region of tilted implantation to analyze the detailed peri-implant bone remodeling response of TNTZ compared with TC4. This was done to explore the performance of mechanobiologically optimized tilted implant materials for clinical tilted implant therapy (Fig. 1).

2. Materials and methods

2.1. Implant preparation and characterization

The Ti–35Nb–2Ta–3Zr (wt. %) biomedical alloy was prepared by arc-melting of high-purity elemental constituents (99.5 wt % Ti, 99.6 wt % Nb, 99.9 wt % Ta and 99.8 wt % Zr) under an argon atmosphere, the ingots of Ti–35Nb–2Ta–3Zr were cast to 7.7 mm thick rectangular samples using a vacuum furnace. To investigate the effects of deformation extent and pressing temperature on the Ti–35Nb–2Ta–3Zr biomedical alloy's microstructures and performances, samples were pressed at various temperatures (300 °C, 500 °C, 700 °C, 900 °C, and 1000 °C) for 50 min, then they were deformed in a multiple-stage hot rolling process resulting in up to 35%, 55%, and 80% thickness reduction. Prior to all the measurements, each sample was polished using silicon carbide papers up to 1000 grits and then polished by colloidal SiO_2 on a Struers MD-chem polishing pad according to standard metallographic procedures. Finally, samples were etched by a Kroll's etchant (30 vol % nitric acid, 5 vol % hydrofluoric acid and 65 vol % water) for 20 s.

Tensile tests were carried out on Zwick T1-Fr020TN materials testing machine at room temperature. In this regard, the ultimate tensile strength (UTS) of the series of Ti–35Nb–2Ta–3Zr alloys were examined, and the elastic modulus of the TNTZ was measured using a three-point bending test. Microstructure observations of samples were examined by JEOL JEM-2100EX transmission electron microscopy (TEM). A sample having the most optimized low elastic modulus Ti–35Nb–2Ta–3Zr alloy (elastic modulus: 47.63 GPa), abbreviated as TNTZ, was selected for further finite element analysis and *in vitro* and *in vivo* biological studies. The surface hydrophobicity of the TNTZ and TC4 implant samples was measured by a contact angle goniometer (SL200B, USA). The surface roughness of TNTZ and TC4 samples were detected using 3D laser scanning confocal microscope (LCM, VK-X 110, Japan).

2.2. Finite element model

The commercial finite element (FE) package Abaqus/Explicit (software version 6.8, USA) was used to model the mechanical behaviors of implants and their peri-implant bone in the present study. The peri-implant bone was modelled and intended to resemble the edentulous alveolar bone, the thickness of cortical bone was adjusted at 1 mm according to the Lekholm and Zarb classification (for bone types III and IV), and the rest comprised trabecular bone [22]. The implant's contour has 10.0 mm length and 3.3 mm diameter referring as a standard plus implant (RN, Straumann® SLA, Switzerland). The properties of the materials used in the FE model were obtained from the literature and this work (Table 1) [22–24], and all materials were assumed to be

homogeneous, isotropic and linearly elastic [23]. Implants were loaded in the 3D state with forces of 10 N at an angle of 45-degree in a disto-mesial direction. The loading was designed based on previous studies [25–27], and its application point was placed on the center of the implant upper surface. The 3D geometrical model of the implant and peri-implant bone was imported into ABAQUS software for finite element analysis, as shown in Fig. 1. The element type of the model was three-dimensional four node element (C3D4). The total number of nodes was 20869, and the total number of elements was 120299. The boundary condition was set as fixed for all translations at the bottom of bone. Fully bonded contact was assumed between bone and implant [10]. To obtain a thorough understanding of stress distribution, Von Mises stress was analyzed [28,29]. Values of Von Mises stress were probed at evenly 60 layers (total 600 distributed sites) in regions of interest (ROI) of peri-implant bone.

2.3. Cell biocompatibility in vitro experiments

Osteoblast cell culture mouse pre-osteoblast cells (MC3T3-E1; Cell-bank of the Chinese Science Academy, China) were cultured in α-modified Eagle's minimum essential medium (α-MEM) (Hyclone, Logan, USA) supplemented with 10% FBS (Fetal Bovine Serum, Gibco) and 1% penicillin/treptomycin at 37 °C in an atmosphere containing 5% CO_2 and 95% humidity.

2.3.1. Cell adhesion

MC3T3-E1 cells were seeded onto the samples in 48-well plates at a density of 4×10^4 cells per well. After 24 and 48 h, the cells on the samples were fixed with 4% paraformaldehyde and then incubated with DAPI (Sigma-Aldrich). Next, the cells adhesion was analyzed with a confocal laser scanning microscope (CLSM, Leica TCS SP5, Wetzlar, Germany). Finally, the cell numbers were counted in five random fields on each sample using ImageJ software (NIH, Bethesda, USA).

2.3.2. Cell morphology

The spreading behavior and cytoskeletal arrangement of osteoblasts seeded onto the samples were examined at 24 h–48 h MC3T3-E1 cells were seeded onto each sample in 48-well plates at a density of 1×10^4 cells per well. At each time point, the cells were fixed with 4% paraformaldehyde and permeabilized with 0.1% Triton X-100. Then the cells were incubated with rhodamine-phalloidin (Biotium, Hayward, USA) and DAPI. Finally, the morphology of the cells was examined using a CLSM.

2.3.3. Cell viability

The viability of cells was determined using a CCK8 assay according to the manufacturer's instructions. MC3T3-E1 cells were seeded onto each sample in 48-well plates at a density of 4×10^4 cells per well for 24, 48 and 72 h. Then ten microliters of CCK8 buffer (Dojindo, Japan) were added to each well, and cells were incubated at 37 °C for an additional 2 h. The absorbance was then measured at a wavelength of 450 nm (650 nm reference) on an ELX800 absorbance microplate reader (Bio-Tek, Winooski, USA). Cell viability was calculated relative to control using the following formula: (experimental group OD-zeroing OD)/control group OD-zeroing OD).

2.3.4. Osteogenic differentiation

For osteogenic differentiation, MC3T3-E1 cells were seeded onto each sample in 48-well plates at a density of 4×10^4 cells per well and cultured in osteogenic media (Cyagen, Santa Clara, USA) for 7 and 21 days. Alkaline phosphatase (ALP) staining and ALP activity were determined using an Alkaline Phosphatase Color Development Kit (Hongqiao, Shanghai, China) and an Alkaline Phosphatase Detection Kit (Jiancheng Bioengineering, Nanjing, China) according to the manufacturer's suggested protocol. Calcium accumulation was detected via 2% alizarin red staining (ARS, Sigma-Aldrich), and calcium levels were then

Table 1
The material properties of different parts of the model.

Type of material	Young's modulus (MPa)	Poisson's ratio	Reference
TC4 implant	110,000	0.35	[22]
TNTZ implant	47,630	0.35	This work, [23]
Trabecular bone	500	0.3	[23,24]
Cortical bone	15,000	0.3	[23,24]

measured using 100 mM cetylpyridinium chloride for 10 min to solubilize and release the calcium-bound alizarin red into solution. The data was expressed as the absorbance at 570 nm of the released alizarin red (detected using a ELX800 absorbance microplate reader). The staining pictures were taken using a digital microscope (keyenceVHX-6000, Japan).

2.4. Animal in vivo experiments

2.4.1. Implant fabrication, animal surgery, and sample processing

For *in vivo* study, the implants were made from TNTZ and TC4 samples by subtractive manufacturing and were simulated the shape of a standard plus implant (RN, Straumann® SLA, Switzerland) with 10.0 mm length and 3.3 mm diameter. The surface of implants was polished as the same method mentioned in 2.1. The experimental outline of this study was shown in Fig. 1. Tilted implantations with load were placed in the iliac crests of goats. Four healthy mature female goats (26-30 months of average age, weighting 40-60 kg) were selected. All processes were conducted following ARRIVE guidelines and National Research Council's Guide for the Care and Use of Laboratory Animals and approved by the Institutional Animal Care and Use Committee of the Ninth People's Hospital, Shanghai Jiao Tong University School of Medicine (SH9H-2021-A92-1, acceptance date: 2021-05-24). The goats were housed in individual pens and an adequately ventilated 12h light/dark cycle environment (temperature 20-30 °C, humidity 50%) 1 week before surgery. The goats were stopped feeding 12 h before surgery, and then were anesthetized by intravenous injection of 2.5% Pentobarbital (1–2 mg/kg). Surgery was performed under 3% isoflurance inhalation anesthesia and sterile conditions. To reduce the risk of peri-operative infection, the goats were injected penicillin sodium intramuscularly twice a day, 80000 U/time before, during and 3 days after surgery. In addition, the goats were received Pethidine (2 mg/kg) to relieve pain three times a day.

The surgical procedure was performed as described in detail by Schouten 2010 [30]. In brief, a transverse skin incision was made in a lateral direction, starting from the posterior superior iliac spine toward the anterior superior part of the iliac crest on both sides of the vertebral column. After separating the soft tissues, the periosteum was separated aside, and the iliac crest was fully exposed. Implant holes drilling were performed using implant drills (Straumann®, Switzerland)) and motor system (NOUVAG MD11, Germany) with low rotational speed (800-1200 rpm) and continuous external cooling with sterile saline solution. Subsequently, four pilot holes were made in the left and right iliac crest using the pilot drill (diameter 2.0 mm), and drilled through the surgical guide in a tilted direction with 45° to the bone plane, then gradually widened the holes (depth 10 mm) with a diameter of 2.8 mm standard drills. The distance between the holes was 5–6 mm. Every animal received four implants in each iliac crest, and TNTZ and TC4 implants were placed according to a randomization schedule by Schouten 2010 [30]. A total of 32 implants were placed using a motor system with low rotational speed (800 rpm) at an angle of 45-degree to the bone plane, and insertion torque values over 15 Ncm. After implant placement, implants were connected to load applications by orthodontic Ni–Ti spring (VectorTas, Ormco, Italy), miniscrews (Cibei, China) and wires (Shinva, China). A static load of 10 N was controlled by a dynamometer (G&G, China) and applied in each tilted implant with vertical orientation to the bone plane. According to the literature, the load delivered by Ni–Ti springs remains constant for the period of this study [31]. And to avoid the bending moment of the load applications, the Ni–Ti springs were kept straight. Finally, the soft tissue layers and skin were closed with 4-0 vicryl sutures (Jinhuan, China). After 3 weeks of implantation, all four goats were euthanized and the specimens from the iliac crest were fixed in 4% formaldehyde solution (48 h) and placed in 70% ethanal for further analysis.

2.4.2. Sequential fluorescent labeling

For recording the healing and remodeling process of the peri-implant bone, the polychrome sequential fluorescent labeling assay was set at day 7 and day 17 post implantation. Two different fluorochromes were intraperitoneally administered into the goats at a sequence of 15 mg/kg Calcein and 20 mg/kg Alizarin Red S, respectively (Fig. 1).

2.4.3. Routine blood test

Routine blood tests were performed before surgery and before euthanasia. For this procedure, 5 mL of whole blood was collected from the jugular vein of each goat in an EDTA tube and the hematological parameters were determined by Auto Hematology Analyzer (BC-2800Vet®, Hamburg, Germany). The following parameters were evaluated: white blood cell (WBC), red blood cell (RBC), hemoglobin (HGB), hematocrit (HCT), mean corpuscular volume (MCV) and mean corpuscular hemoglobin concentration (MCHC).

2.4.4. Analysis of XRM images and bone morphometry indices

The bone blocks of iliac crest containing one implant each and at least 3 mm peri-implant bone were cut off by a cutting/grinding system (Exakt Apparatebau, Hamburg, Germany) and wrapped in parafilm, then the specimens were scanned on X-ray Microscopy (Xradia Versa 520, Carl Zeiss XRM, USA) at a pixel size of 10 μm (voltage: 80 kV, power: 7 W, exposure time: 2 s). According to the manufacturer's instructions, a filtered secondary reference was applied to modify the beam for both the reference and the tomography during the original scan to reduce the diffuse artifacts in metal implant specimen images. Next, XMReconstructor (Carl Zeiss, USA) was used to reconstruct the 2D images of the implants and the peri-implant bone. Finally, bone area/total tissue area (B.Ar/T.Ar), trabecular number (Tb.N) and trabecular spacing (Tb.Sp) were determined using CTAn (Skyscan, Kontich, Belgium) analysis software in the related ROIs. In particular, the values of B.Ar/T.Ar were calculated from evenly 60 layers at ROIs of peri-implant bone, which were corresponded to the same layers of Von Mises stress probe values in FE analysis. The curve and related slope for variation of B.Ar/T.Ar was calculated using the GraphPad Prism 9.0 statistical software package (GraphPad Software, USA), results were showed with a layer-by-layer quantitative correlation of the FE and X-ray Microscopy (XRM) analysis of peri-implant bone.

2.4.5. Histological and histomorphometrical evaluation

After the XRM scan, the specimens (non-decalcified) for histological processing were gradually dehydrated in ethanol solutions from 70% to 100% and subsequently embedded in methyl methacrylate (MMA, Sigma-Aldrich). After enough polymerization of the MMA specimens, 100 μm thick longitudinal sections of the implants were prepared using microtome technique (SP1600, Leica, Wetzlar, Germany), and then the sections were ground and polished to 20 μm thickness for histological evaluation. Sequential fluorescence labeling observation was performed under CLSM with × 200 magnification. The used excitation/emission wavelengths to observe the chelating fluorochromes respectively were 488/520 nm and 543/620 nm for calcein (green) and alizarin red S (red). Three section slides from each specimen were selected for histomorphometric analysis. Using calcein and alizarin red as labels, the mean interlabel width (Ir. L. Wi) was measured by averaging the distances between points, randomly selected from 5 intervals using ImageJ software, and the trabecular bone dynamic parameters MAR (The mean Ir. L. Wi/interval period, μm/day) were calculated at ROIs. Afterwards, the sections stained with Van Gieson's picro-fuchsin (Sigma-Aldrich) and visualized the bone-implant interfaces and bone response using an inverted microscope (Nikon eclipse TS2. Japan), the area of new bone formation was quantified using ImageJ software [32].

2.5. Statistical analysis

All the experiments were performed at least in triplicate and the

values were presented as mean $\pm$ standard deviation. The data were analyzed by GraphPad Prism 9.0 statistical software package (GraphPad Software, USA). Mann-Whitney test was used to compare the differences between two independent groups. Two-way ANOVA with Bonferroni post-test was used for comparisons among multiple groups. Significant differences between groups were expressed as: $*p < 0.05$, $**p < 0.01$, and $***p < 0.001$.

3. Results

3.1. Mechanical properties optimization and characterization of Ti–35Nb–2Ta–3Zr tilted implant materials

3.1.1. Mechanical properties of Ti–35Nb–2Ta–3Zr alloys

The mechanical properties of Ti–35Nb–2Ta–3Zr alloys subjected to hot rolling with the deformation extent of 35%–80% and rolling temperature of 300 to 1000 °C were summarized in Fig. 2A. In general, the ultimate tensile strength (UTS) continuously decreased with the increment of temperature. In contrast, the elastic modulus has a low level in a specific temperature range (700-900 °C). Relatively ideal mechanical properties were obtained when Ti–35Nb–2Ta–3Zr subjected to hot rolling with (35%–55%) deformation at a temperature of 700 °C and 900 °C. In this regard, the lowest elastic modulus of Ti–35Nb–2Ta–3Zr was 47.63 GPa under 35% of deformation and 900 °C rolling temperature.

Fig. 2B showed the comparison of elastic modulus and UTS of various TiNbTaZr biomedical alloys fabricated by plastic deformation methods

[33–40] in typical recent studies. The Ti–35Nb–2Ta–3Zr (900 °C, 35%) in this work exhibited an excellent combination of elasticity modulus and strength properties among these alloy systems (Fig. 2B, Table S1). Such comparison also suggested that hot rolling with (35%–55%) deformation at a temperature of 700 °C and 900 °C are promising approaches to synchronously enhance mechanical properties of Ti–35Nb–2Ta–3Zr for tilted implantation used.

3.1.2. Microstructure of Ti–35Nb–2Ta–3Zr (900 °C, 35%) alloy

To clarify the contribution of underlying microstructures on mechanical properties of Ti–35Nb–2Ta–3Zr, specimens of Ti–35Nb–2Ta–3Zr (900 °C, 35%) were further examined using TEM tests. Fig. 3A and B presented bright and dark field TEM images under different zone axes. Fig. 3A was achieved under [01-1]β, while Fig. 3B was achieved under [01-2]β. Dislocation and needle-shaped precipitates were observed. Needle-shaped precipitates had about tens of nanometers length. Meanwhile, precipitates achieved very limited width, showing a high aspect ratio. Dislocation was obviously observed at position of needle-shaped precipitates, indicating that the dislocation defects are conducive to the nucleation of precipitates. Both ω and α'' martensite diffraction spots were confirmed in the corresponding selected area electron diffraction (SAED) pattern. No obvious characteristic difference between precipitates was detected, indicating coexistence of ω and α'' martensite.
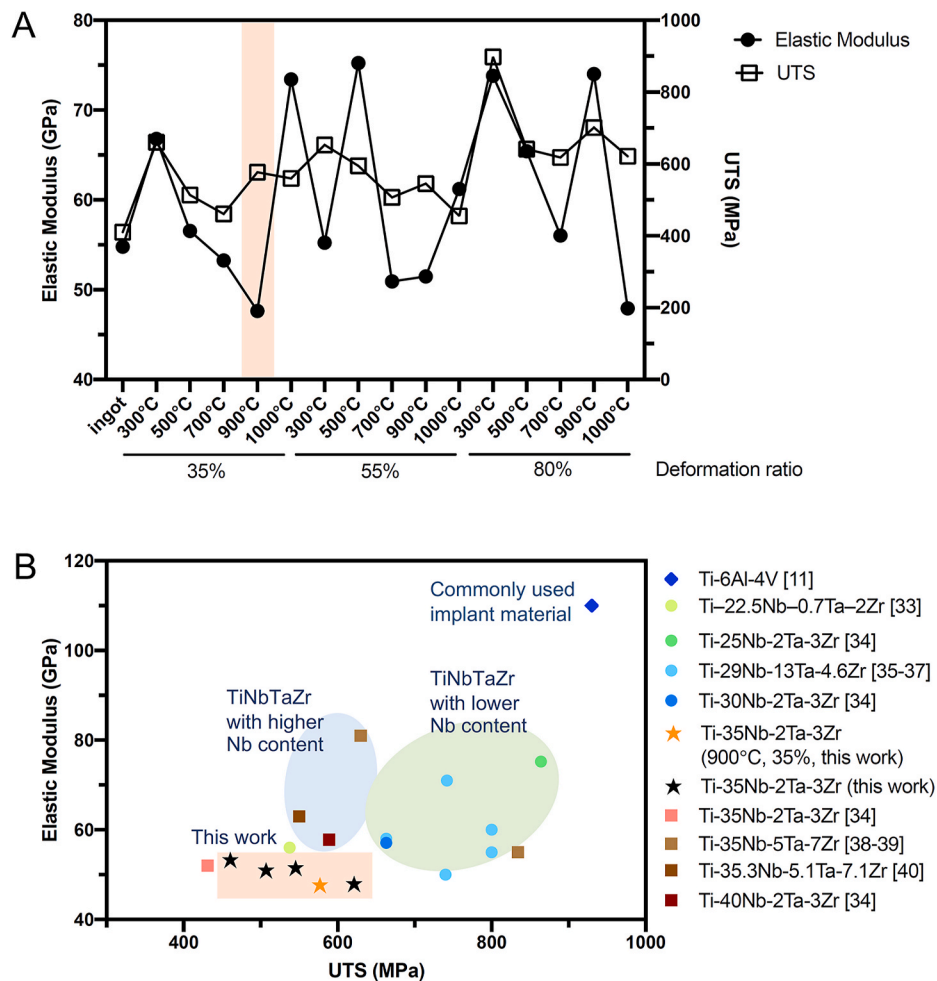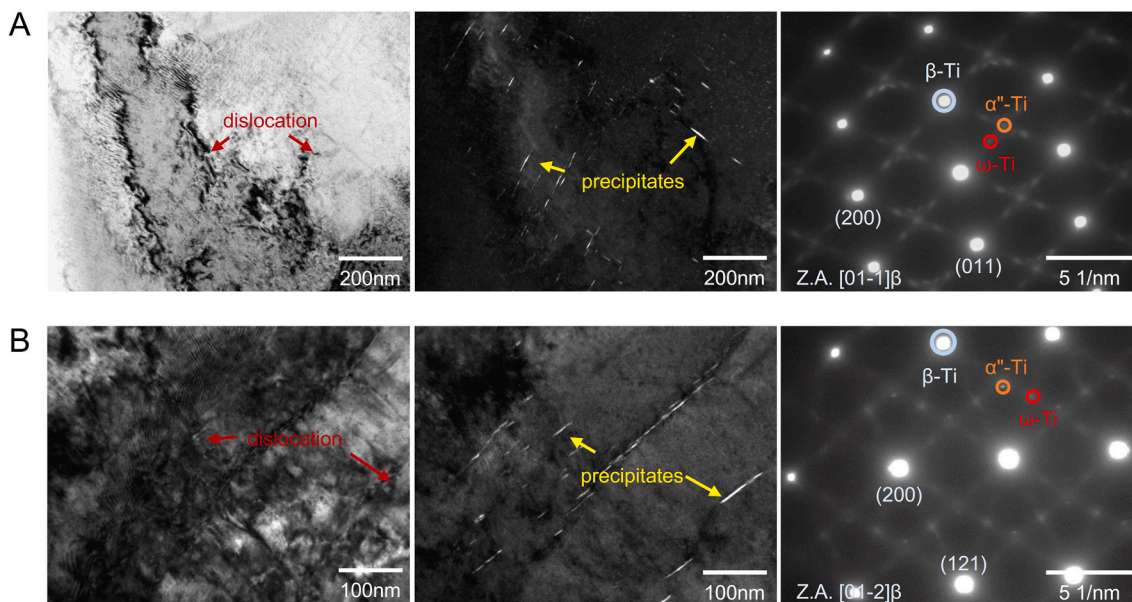

Fig. 2. Mechanical characterization of Ti–35Nb–2Ta–3Zr alloys. A. Elastic modulus and UTS of Ti–35Nb–2Ta–3Zr alloys subjected to hot rolling with gradient processing parameters. B. The comparison of elastic modulus and UTS of Ti–35Nb–2Ta–3Zr alloys with typical recent studies.

Fig. 3. Microstructure characterization of Ti–35Nb–2Ta–3Zr alloy (900 °C, 35%). A. TEM images of bright field, dark field image at low magnification and its corresponding SAED pattern. B. TEM images of bright field, dark field image at high magnification and its corresponding SAED pattern.

3.1.3. Hydrophilicity and surface roughness of Ti–35Nb–2Ta–3Zr (900 °C, 35%) and TC4 alloy

The hydrophilicity of implant materials was measured by contact angel, the results indicated that the hydrophilicity of Ti–35Nb–2Ta–3Zr (900 °C, 35%) implant materials were not apparently different compared to TC4 (Fig. S1). And the average surface roughness (Ra) of Ti–35Nb–2Ta–3Zr and TC4 were 0.345 and 0.375 μm, respectively (Table, S2).

In total, Ti–35Nb–2Ta–3Zr (900 °C, 35%) presented the optimized mechanical properties and hydrophilicity in this work. To further investigate the mechanobiological characteristic of Ti–35Nb–2Ta–3Zr (900 °C, 35%. Later abbreviated as TNTZ) for clinical tilted implantation, the implant material TC4 was selected as a comparison in subsequent mechanical and biological studies.

3.2. The cell biocompatibility of TNTZ and TC4 implant materials in vitro studies

3.2.1. Cell attachment, spreading and proliferation

The CLSM images of cells nuclei and its quantitative analysis presented cell attachment on the samples in Fig. 4A, the number of MC3T3-E1 cells on TNTZ was more than on TC4 at 24 h. After 48 h of culture, cells had a similar attachment on the TNTZ and TC4 samples. Fig. 4B showed the cell morphology and spreading on the samples. Cells actin filaments linking adjacent cells on all the samples displayed an increasing tendency from 24 h to 48 h. In addition, cells grown on the TNTZ and TC4 samples were polygonal and clustered at 24 h, and the spreading pattern of cells became more dispersive at 48 h. The proliferation of MC3T3-E1 cells cultured on the samples were analyzed using a CCK-8 assay as shown in Fig. 4C. Cells grown on the TNTZ and TC4 both displayed a persistent increasing proliferation tendency from 24 h to 72 h. Besides, cells grown on the TNTZ group exhibited no significant difference from the TC4 group in the proliferative trend.

3.2.2. ALP, alizarin red staining and quantitative analysis

Fig. 4D presented the results of osteogenic differentiation analysis of MC3T3-E1 cells on the samples. The ALP staining and its activity on TNTZ were higher than TC4 at 7 d. While the alizarin red staining as well as its quantitative analysis of the TNTZ and TC4 showed the generation of calcium nodules with no significant difference at 21 d.

Collectively, the results of *in vitro* studies indicated that TNTZ has similarly excellent biocompatibility as TC4 implant material.

### 3.3. Combination of finite element (FE) and in vivo analysis for TNTZ and TC4 tilted implantation

3.3.1. Finite element model and animal in vivo model

Based on the conception of reverse engineering, the finite element (FE) analysis techniques were used to mimic tilted implantation under specific loading conditions of 10 N and investigate its effects on stress distribution in tilted implants and peri-implant bone. To determine corresponding peri-implant bone remodeling *in vivo*, a tilted implantation model was performed with the same static load of 10 N in the iliac crests of goats (Fig. 5A–B). Surgical procedures were performed without complications. All animals remained in good general health during the experimental period without any clinical signs of discomfort or wound complications. The routine blood tests of all animals were within the normal range before surgery and before euthanasia. After 3 weeks of implantation, no macroscopic adverse tissue reactions were apparent around the implant sites and all implants were retrieved.

3.3.2. Stress distribution and related bone characterization for TNTZ and TC4 at ROIs

Based on the trajectorial theory, the organization of trabecular bone regard as the cornerstone of Wolff's Law, and the pattern and orientation of trabeculae are transformable with alterations in loading pattern, while its patterning represented the average regime experienced by the bone [41], so we focused on the trabecular peri-implant bone in order to explore its biological features under the stress distribution of tilted implantation. According to the action mode of load transduction, we divided the region of peri-implant bone related to the components of stress to the compressive side and tensile side [42], Fig. 5A displayed the selected regions of interest (ROIs) illustration within the peri-implant bone for tilted implantation model.

With a layer-by-layer quantitative correlation of the FE and X-ray Microscopy (XRM) analysis of peri-implant bone, both the results of TNTZ and TC4 suggested that the values of stress intensity gradually declined by degrees from the lower 1/3 to middle 1/3 region of peri-implant bone, and the corresponding bone area tend to be relatively stable at lower 1/3 region and decreased slowly at middle 1/3 region in
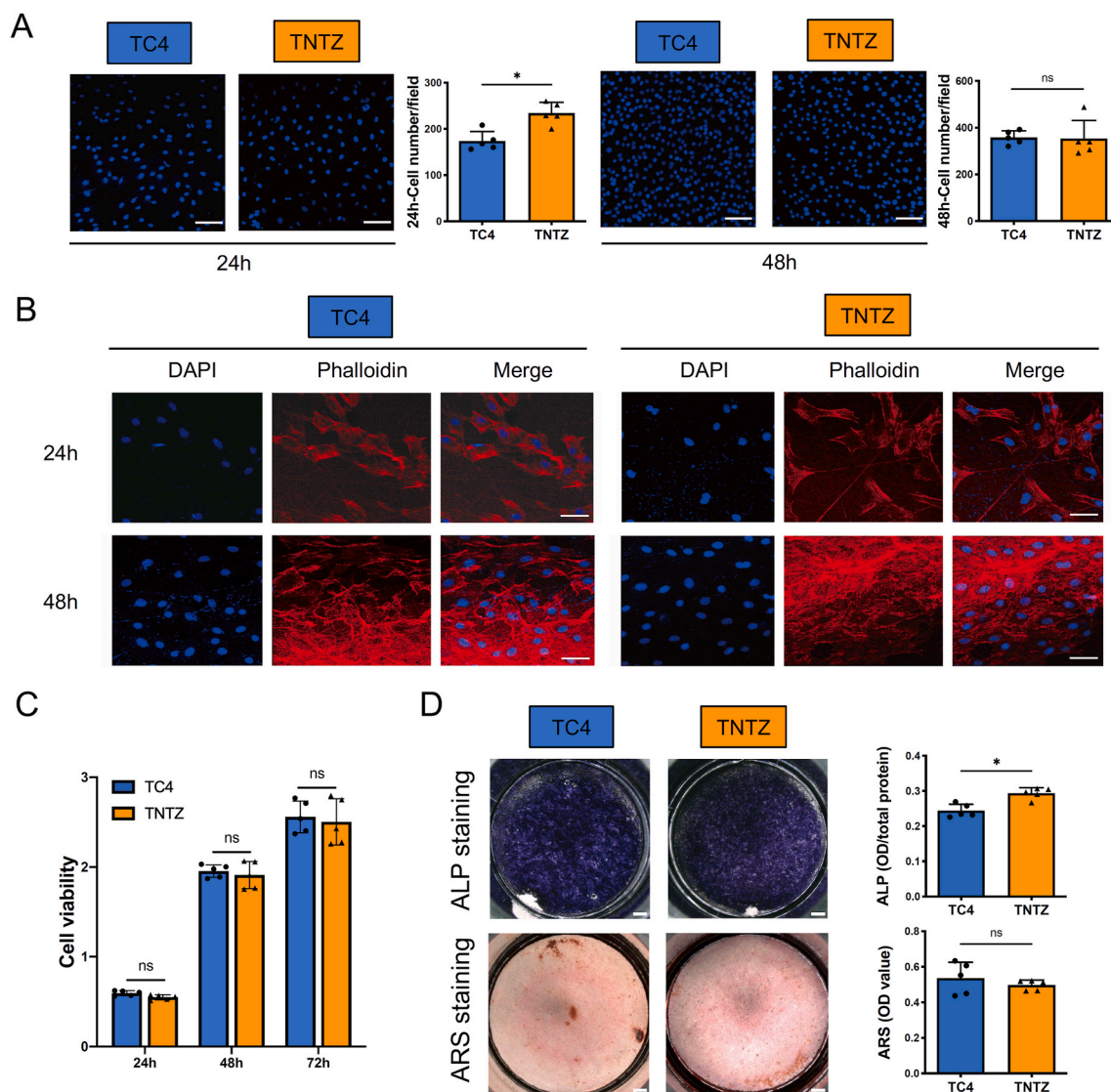
Fig. 4. *In vitro* studies of the cell biocompatibility. A. CLSM images and quantitative evaluation for MC3T3-E1 cells adhesion and proliferation on TC4 and TNTZ at 24 and 48 h (Scale bar: 100 μm n = 5, Mann-Whitney test). B. CLSM images for the cytoskeleton of MC3T3-E1 cells spreading on TC4 and TNTZ at 24 and 48 h (Scale bar: 50 μm). C. CCK-8 analysis for the proliferation activity of MC3T3-E1 cells on TC4 and TNTZ at 24, 48 and 72 h (n = 5, Two-way ANOVA with Bonferroni post-test). D. The alkaline phosphatase (ALP) and alizarin red staining (ARS) and quantitative evaluation for MC3T3-E1 cells of TC4 and TNTZ at 7 d and 21 d respectively. (Scale bar: 1 mm n = 5, Mann-Whitney test). All data are represented as mean ± SD. *p < 0.05. NS, no significance. (For interpretation of the references to colour in this figure legend, the reader is referred to the Web version of this article.)

both the compressive side and tensile side of TNTZ and TC4 peri-implant bone (Fig. 5C–D, Figs. S2A–B). The slope for variation of the bone area was similar between TNTZ and TC4 at lower 1/3 and middle 1/3 region (Fig. 5F). While at upper 1/3 region, the values stress intensity of TNTZ and TC4 peri-implant bone were both under the "disuse-mode remodeling threshold" of bone according to Frost's mechanostat theory [43], suggested that there was not enough stress for bone remodeling in the upper 1/3 region in both TNTZ and TC4 peri-implant bone, that's to say the upper 1/3 region was "lower stress" (Fig. 5C–D, Fig. S3). At this region, the corresponding bone area showed a sharp decrease in TC4 but a slowly decreasing trend in TNTZ (Fig. 5C–E), and the slopes for variation of the bone area in TC4 were significantly larger than in TNTZ at upper 1/3 (Fig. 5F). Additionally, the result of the FE calculation showed that the mechanical stress mainly concentrated on the external middle region of implants near the interface with the bone, and TC4 implant born much more stress than TNTZ implant (Fig. S4). Therefore, the results suggested that the TNTZ implant improved load transduction and increased bone area comparing to the TC4 implant in the tilted

implantation model, especially in the upper 1/3 region of peri-implant bone which was "lower stress".

3.4. The peri-implant bone remodeling in the "lower stress" region

To further investigate mechanobiologically optimized implant materials for tilted implantation, it was focused on the detailed bone remodeling characterizations at upper 1/3 region which was "lower stress" in the peri-implant bone. The overview transaxial images of XRM and VG staining showed the bone area of peri-implant bone in TNTZ was more than that in TC4 (Fig. 6A–B). Coinciding with the tendency of bone area, the bone static parameter Tb.N and the new bone formation of TNTZ were higher than TC4, and the bone static parameter Tb.Sp of TNTZ was much lower than TC4 (Fig. 6A–B). Similarly, the dynamic parameter MAR of TNTZ were higher values than TC4 (Fig. 6C). In addition, the bone response in the tensile and compressive sides for TNTZ and TC4 were further compared, except the Tb.N and MAR parameters of TNTZ, the bone healing and remodeling were not obviously
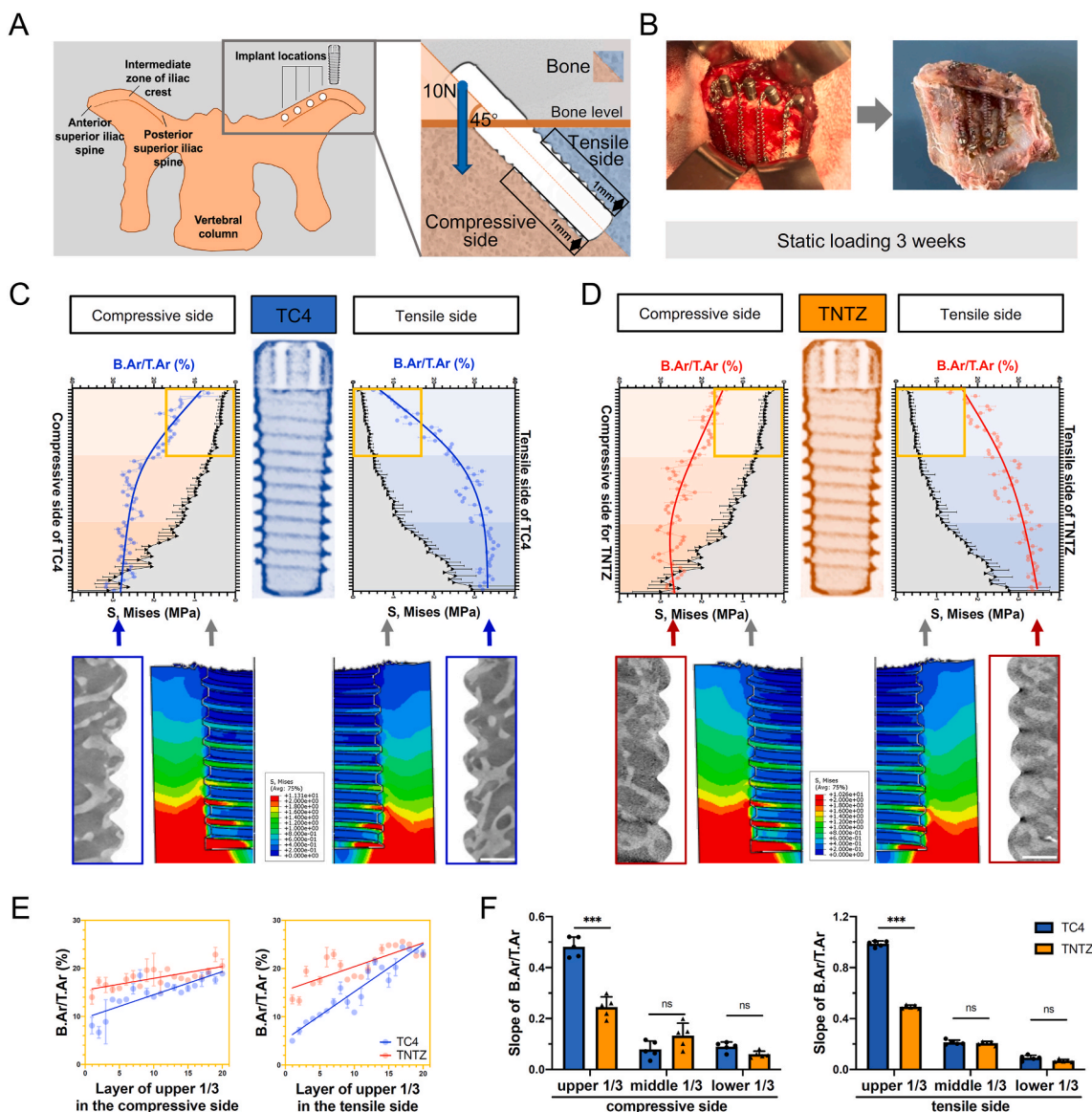
Fig. 5. Combination of finite element (FE) and *in vivo* analysis. A. The regions of interest (ROIs) illustration within the peri-implant bone in the compressive and tensile side. B. Representation of tilted implantation with load in iliac crest of goat. C. Layer-by-layer quantitative correlation of Von Mises stresses from FE analysis and bone area/total tissue area (B.Ar/T.Ar) from XRM analysis for TC4 at ROIs (Scale bar of XRM sagittal image is 1000 μm). D. Layer-by-layer quantitative correlation of Von Mises stresses from FE analysis and B.Ar/T.Ar from XRM analysis for TNTZ at ROIs (Scale bar of XRM sagittal image is 1000 μm). E. The variation of percent trabecular area for TC4 and TNTZ at upper 1/3 region. F. The variation slope of percent trabecular area for TC4 and TNTZ (n = 5, Two-way ANOVA with Bonferroni post-test). All data are represented as mean ± SD. ***$p < 0.001$. NS, no significance.

different between two sides in the upper 1/3 region (Fig. S5). In total, the bone healing and remodeling of TNTZ were better than TC4 at upper 1/3 region, which was coincided with the tendency of overalls stress values for TC4 and TNTZ by FE analysis. Compared to TC4 implant, TNTZ with its elastic modulus best match to that of peri-implant bone showed better mechanobiological characteristics in tilted implantation models with respect to improved implant-bone load transduction and enhanced bone remodeling around the "lower stress" region as determined by static and dynamic parameters of bone.

4. Discussion

The aim of this study was to optimize mechanical properties of tilted implant material and determine the stress distribution as well as related peri-implant bone remodeling in the tilted implantation model. The TNTZ implant was compared with clinical commonly used TC4 implant to explore the optimized and customized mechanobiological design in

clinical tilted implant therapy. And the results showed that TNTZ implant with an improved mechanobiological effect presented an improved load transduction and bone remodeling response.

4.1. Mechanobiologically optimized implant material design for the need in tilted implantation therapy

Among all titanium alloys, α + β type alloy Ti–6Al–4V, has be widely used in biomedical applications. However, despite its biomechanical incompatibility that impedes load transduction, it contains elements V and Al that are toxic to the human body [44]. In order to satisfy the above conditions, β-Titanium alloys are reported to be an excellent candidate for biomedical dental applications, with the addition of non-cytotoxic and β phase-stabilized elements such as Nb, Ta, Zr, Mo, and Sn in titanium alloys [45], while the element content can also affect the elasticity of these alloys [46]. Nobuhito et al. [47] revealed that Ta and Nb content could influence the mechanical properties of TiNbTaZr,
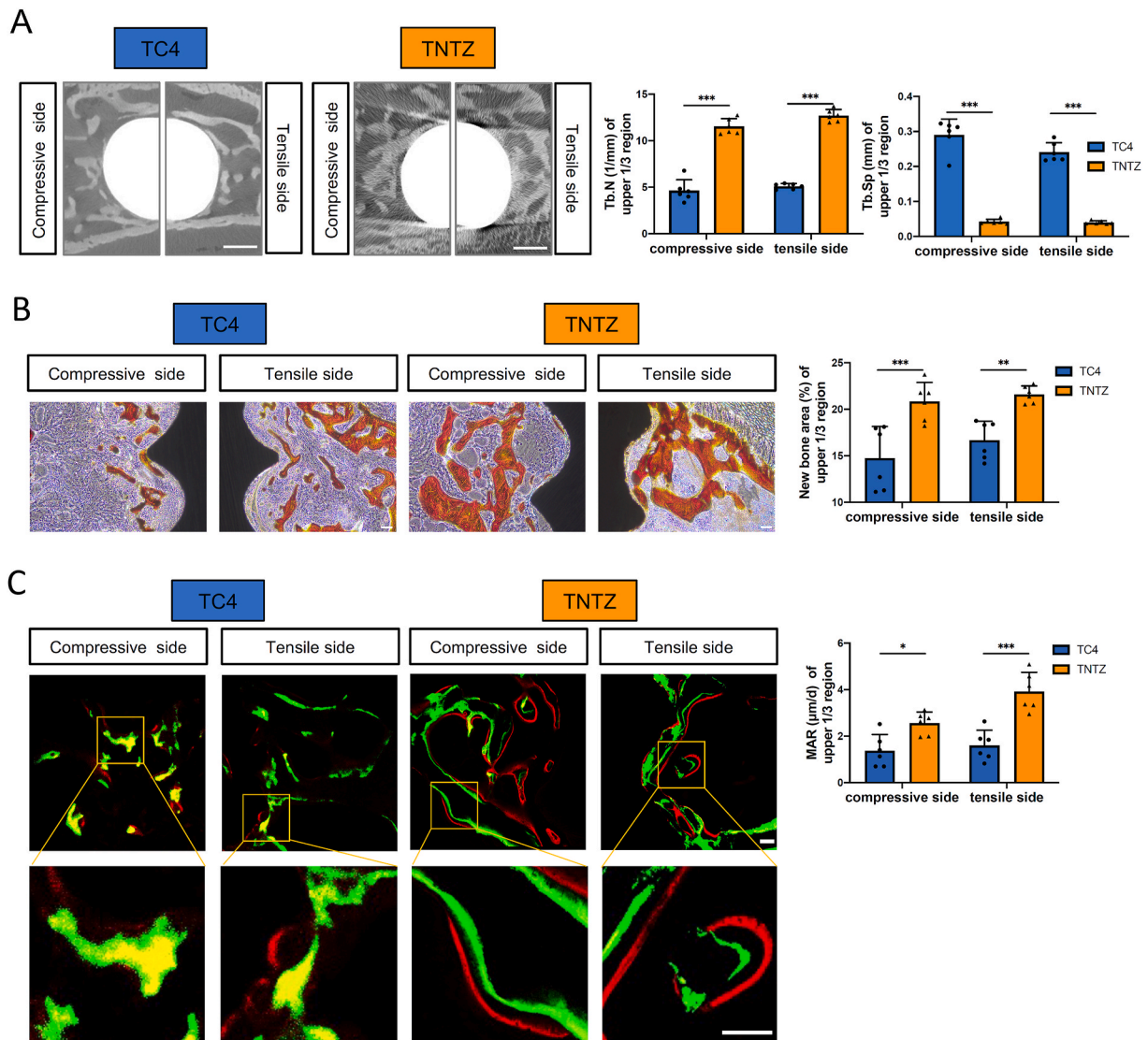
Fig. 6. The peri-implant bone remodeling in the "lower stress" region. A. XRM transaxial image for TC4 and TNTZ (scale bar: 1000 μm). Trabecular number (Tb.N), trabecular spacing (Tb.Sp) at ROIs (n = 6, Two-way ANOVA with Bonferroni post-test). B. Van Gieson's picro-fuchsin (VG) staining for TC4 and TNTZ (scale bar: 100 μm n = 6, Two-way ANOVA with Bonferroni post-test). New bone formation at ROIs (n = 6, Two-way ANOVA with Bonferroni post-test). C. Sequential fluorescent labeled images for TC4 and TNTZ, showing calcein (green) and alizarin red (red) (scale bar: 100 μm n = 6, Two-way ANOVA with Bonferroni post-test). Bone mineral apposition rate (MAR) analysis at ROIs. All data are represented as mean ± SD. $*p < 0.05$, $**p < 0.01$, $***p < 0.001$. (For interpretation of the references to colour in this figure legend, the reader is referred to the Web version of this article.)

and observed low elastic modulus of Ti alloys with 10 mass % of Ta and high modulus of elasticity for these alloys with 0 and 20 mass % of Ta addition.

Furthermore, the plastic deformation process affected the microstructure of β-type Ti alloys. It is known that deformation products that are formed during plastic deformation processes could induce substantial changes in mechanical properties [46]. Thus, the simulations were performed on five different hot rolling temperatures with three deformation rates to find which of the mentioned conditions is the most likely to produce the desired mechanical properties of TNTZ alloy. When the rolling temperature was at 900 °C and deformation ratio at 35%, the TNTZ alloy achieved the optimized elastic modulus of 47.63 GPa with enough strength (Fig. 2A–B), comprised ω and α'' phases (Fig. 3A–B). With significant deformation during the rolling process, the reaction between dislocations occurred which is confirmed in bright field images. A high level of stress was restored and provided the driving force for β to ω transformation. On this basis, ω phase could further transmit into α'' martensite, which indicated that two phases were in the same position

[48]. Since ω to α'' transformation is reversible with the change of stress level [49], transition to α'' was difficult to carry out thoroughly. The α'' martensite tended to be observed together with ω phase instead of α'' itself. A similar study was showed by Li et al. [50], in which improving the mechanical properties of the Ti–Nb–Zr alloys is related to the presence of the ω phase, since ω is a hard and brittle phase which could improve the strength of the β phase. Besides, due to the coherent interface between the ω phase and β matrix, the reaction of nanobands with dislocations also contributed to the strengthening effect of the ω phase. Liu et al. [51] also revealed that the lattice expansion by Nb and Zr addition as well as the presence of a few of α'' martensite, might be responsible for the low modulus of Ti–Nb–Zr alloys achieved. TNTZ alloy in this work has typical β matrix diffraction patterns. Therefore, elements with large atomic numbers (Nb, Ta, Zr) were supposed to have a lattice expansion effect, instead of a lattice-altering effect. Meanwhile, stress induced martensite contributed to modulus reduction during reorientation. Therefore, an appropriate plastic deformation process and proper selection of alloying elements with the appropriate compositions

are highly essential to achieve a customized design of TNTZ alloys with enough strength, low elastic modulus and excellent biocompatibility for clinical tilted implantation.

4.2. The clinical transformation study of mechanobiological optimized implant material in tilted implantation

In the clinical transformation study, it is crucial to mimic the human edentulous alveolar bone under loading environment. Since the mechanical loading and related load transduction cannot be observed and be difficult to be evaluated within the bone *in vivo*, these evaluations of tilted implantation were conducted with FE analysis, in order to mimic loaded tilted implants in the human edentulous alveolar bone and investigate detailed stress distribution in the different regions of peri-implant bone. Meanwhile, the FE analysis can provide "virtual" results of stress distribution, which is necessary to verify its validity based on the "real" *in vivo* results. Based on the similar physiology, pathology quality and structure conditions to human edentulous alveolar bone [30, 52,53], and take advantages of easy surgical exposure, less stress and quicker recovery for the animals [30,54], the iliac crest of goats was chosen to mimic human alveolar ridge conditions *in vivo* (Fig. 5A–B).

Regarding to this study time point, the early peri-implant bone healing and remodeling stage of the immediate loading on implant was focused [55]. A sequence of peri-implant bone healing and remodeling events started with the period from the primary stability stage to the secondary stability stage of the implant [56], and the primary mechanical stability of implant is gradually transformed to secondary biological stability provided by newly formed bone as osseointegration occurs [57]. Both primary and secondary stability of the implant are associated with the peri-implant bone osteointegration and can be displayed as bone-implant interface strength, while the latter is further influenced by the condition of mechanical loading [53,56]. In addition, the *in vivo* effect of loading on bone may differ according to its biological state, and the interfacial bone may be more sensitive to loading when it is healing or damaged [58]. Therefore, the time point was focused on 3 weeks after implant placement in the present study.

For the evaluation of the *in vivo* bone architecture, the reconstruction of 3D-dimensional information of peri-implant bone can provide for evaluating bone remodeling. However, the common strategies, such as Micro-computed tomography (micro CT) with X-ray tubes and clinical computed tomography (CT), are vulnerable to metal material implants, and streak artifacts in the reconstructed images can severely impair the quantitative analysis of peri-implant bone, especially in the region up to about 200 μm from the implant surface [59,60]. As the ROI regions were selected as the main remodeling zone of peri-implant bone [61], which were very near the implant (Fig. 5B). Therefore, a by nature and non-destructive X-ray Microscopy (Xradia Versa XRM520) with the physical filters was used for the reconstruction of the tilted implantation specimens' images and reduction of the ring artifact in this study. From the XRM images of the goat iliac crest, a well-defined and clear peri-implant trabecular bone structure was in close contact with the implant, and the most orientation of trabeculae was perpendicular channel relative to the long axial of the implant (Fig. 5C–D).

4.3. The interdependent relationships between mechanical characteristics of materials and the features of bone biology

Frost's mechanostat theory relates different levels of mechanical stress to influence bone remodeling response [43]. When mechanical load transfers to the bone, the osteocyte network contributes to the mechanosensory response and regulates the osteoblast-osteoclast axis [62]. In the mechanotransduction processes, occlusal forces are sensed by bone and transformed into biological and biochemical reactions [63]. As a result of this mechanosensing communication stream, the mechanical information within peri-implant bone is presented in the form of bone remodeling. Delgado-Ruiz et al. [64] investigated implant

insertion with immediate loading and observed that the bone density and bone-to-implant contact of the different materials and surfaces implants increased when they were subjected to mechanical loading at 3 months. In our study, a quantitative correlation of the stress intensity value and morphometry indices of peri-implant bone was conducted in a layer-by-layer way in which bone remodeling characterization changes are closely related to the load transduction of implant materials (Figs. 5 and 6).

Previous studies have suggested that stress ranges between 20 and 60 MPa are beneficial for bone remodeling and strengthen the bone, whereas, during below 1-2 MPa, bone disuse-mode takes place and trabecular bone loss increases [65]. In this study, FE analysis suggested the "lower stress" region in the upper 1/3 of implant bone (Fig. 5C–D), in which the bone area decreased sharply (Fig. 5F). Similar to this study, the modulus of elasticity varies between metal and bone leading to load transduction change and stress shielding occur, which caused the proximal peri-implant bone resorption [66]. Regarding, the combination between the changing trend of bone area and stress intensity value in the tilted implant model, our results found that although the stress degree is still under bone disuse-mode threshold by Frost, the peri-implant bone area is incremented when elastic modulus optimized TNTZ implant was used (Fig. 5C–D, Fig. S3). Also, the static and dynamic parameters of bone were comprehensively studied to further verify the better peri-implant bone remodeling response of TNTZ compared to TC4 in the "lower stress" region (Fig. 6A–C). As the limitations of the study, the implants were applied in static 10 N loading and the time point was set at 3 weeks. Future tilted implant studies with multiple parameters, such as forces and time points design, are suggested to reveal the mechanobiological characteristics of TNTZ in more detail. Within the limitations, the results of this study supported the hypothesis that a design of TNTZ implant with a similar elastic modulus to the bone would provide a beneficial mechanical environment for peri-implant bone remodeling in tilted implantation by improving the load transduction effect and enhancing bone remodeling.

5. Conclusion

This study based on the concept of "materiobiology", provided a research basis for the future clinical transformation of mechanobiologically optimized TNTZ material design in tilted implant therapy as well as experience and reference for the application of tilted implants in large-animal experiment. The main conclusions are as follows:

a. The TNTZ alloy samples after plastic deformation processes at 700 and 900 °C temperature and 35-55% deformation ratio exhibited the low elastic modulus (47.63–53.26 GPa) with strength (460.59–576.91 MPa). At a 900 °C temperature and 35% deformation ratio, TNTZ reached the optimized mechanical properties (elastic modulus 47.63 GPa and strength 576.91 MPa) with favorable biocompatibility for tilted implantation.

b. Through mimicking human alveolar bone environment and clinical tilted implant with immediate loading in the mechanical and biological model, it was showed that elastic modulus of implant metals could influence the biological response of peri-implant bone remodeling, while TNTZ implant presented better mechanobiological characteristic both concerning improved load transduction and increased bone area comparing to TC4 implant by layer-by-layer quantitative correlation of the FE and XRM analysis.

c. It was also focused on the peri-implant bone region, which is "lower stress" and combined the static and dynamic parameters of bone, revealing that TNTZ implant enhanced bone remodeling in both new bone formation and mineral apposition speed.

Ethics approval and consent to participate

All animal experiments complied with the animal protocols were

approved by the Institutional Animal Care and Use Committee of the Ninth People's Hospital, Shanghai Jiao Tong University School of Medicine.

CRediT authorship contribution statement

Chuanyuan Mao: Methodology, Validation, Investigation, Writing – original draft, Visualization. **Weijun Yu:** Methodology, Validation, Investigation, Visualization. **Min Jin:** Methodology, Visualization. **Yingchen Wang:** Visualization, Investigation. **Xiaoqing Shang:** Validation, Investigation. **Lu Lin:** Validation, Investigation. **Xiaoqin Zeng:** Conceptualization, Supervision, Funding acquisition. **Liqiang Wang:** Conceptualization, Writing – review & editing, Supervision, Funding acquisition. **Eryi Lu:** Conceptualization, Supervision, Writing – review & editing, Supervision, Funding acquisition.

Declaration of competing interest

The authors declare that they have no known competing financial interests or personal relationships that could have appeared to influence the work reported in this paper.

Acknowledgements

Appendix A. Supplementary data

Supplementary data to this article can be found online at https://doi.org/10.1016/j.bioactmat.2022.03.005.

References

[1] G.E. Romanos, R. Delgado-Ruiz, A. Sculean, Concepts for prevention of complications in implant therapy, Periodontol 81 (2019) 7–17, https://doi.org/10.1111/prd.12278, 2000.

[2] D.A. Atwood, Some clinical factors related to rate of resorption of residual ridges, J. Prosthet. Dent 86 (2001) 119–125, https://doi.org/10.1067/mpr.2001.117609, 1962.

[3] P. Maló, B. Rangert, M. Nobre, All-on-Four" immediate-function concept with Brånemark System implants for completely edentulous mandibles: a retrospective clinical study, Clin. Implant Dent. Relat. Res. 5 (Suppl 1) (2003) 2–9, https://doi.org/10.1111/j.1708-8208.2003.tb00010.x.

[4] P. Maló, M. de Araujo Nobre, A. Lopes, C. Francischone, M. Rigolizzo, All-on-4" immediate-function concept for completely edentulous maxillae: a clinical report on the medium (3 years) and long-term (5 years) outcomes, Clin. Implant Dent. Relat. Res. 14 (Suppl 1) (2012) e139–150, https://doi.org/10.1111/j.1708-8208.2011.00395.x.

[5] C.H.F. Hammerle, L. Cordaro, K.A.A. Alccayhuaman, D. Botticelli, M. Esposito, L. E. Colomina, A. Gil, F.L. Gulje, A. Ioannidis, H. Meijer, S. Papageorgiou, G. Raghoebar, E. Romeo, F. Renouard, S. Storelli, F. Torsello, H. Wachtel, Biomechanical aspects: summary and consensus statements of group 4. The 5(th) EAO Consensus Conference 2018, Clin. Oral Implants Res. 29 (Suppl 18) (2018) 326–331, https://doi.org/10.1111/clr.13284.

[6] E. Bruschi, P.F. Manicone, P. De Angelis, L. Papetti, R. Pastorino, A. D'Addona, Comparison of marginal bone loss around axial and tilted implants: a retrospective CBCT analysis of up to 24 months, Int. J. Periodontics Restor. Dent. 39 (2019) 675–684, https://doi.org/10.11607/prd.4110.

[7] S. Ozan, J. Lin, W. Weng, Y. Zhang, Y. Li, C. Wen, Effect of thermomechanical treatment on the mechanical and microstructural evolution of a β-type Ti-40.7Zr-24.8Nb alloy, Bioact. Mater. 4 (2019) 303–311, https://doi.org/10.1016/j.bioactmat.2019.10.007.

[8] J.B. Brunski, Biomechanical factors affecting the bone-dental implant interface, Clin. Mater. 10 (1992) 153–201, https://doi.org/10.1016/0267-6605(92)90049-y.

[9] D. Ozdemir Dogan, N.T. Polat, S. Polat, E. Seker, E.B. Gul, Evaluation of "all-on-four" concept and alternative designs with 3D finite element analysis method, Clin. Implant Dent. Relat. Res. 16 (2014) 501–510, https://doi.org/10.1111/cid.12024.

[10] F. Azcarate-Velázquez, R. Castillo-Oyagüe, L.-G. Oliveros-López, D. Torres-Lagares, Á.-J. Martínez-González, A. Pérez-Velasco, C.D. Lynch, J.-L. Gutiérrez-Pérez, M.-Á. Serrera-Figallo, Influence of bone quality on the mechanical interaction between implant and bone: a finite element analysis, J. Dent. 88 (2019) 103161, https://doi.org/10.1016/j.jdent.2019.06.008.

[11] M. Kaur, K. Singh, Review on titanium and titanium based alloys as biomaterials for orthopaedic applications, Mater. Sci. Eng. C Mater. Biol. Appl. 102 (2019) 844–862, https://doi.org/10.1016/j.msec.2019.04.064.

[12] S.D. Cook, J.J. Klawitter, A.M. Weinstein, The influence of implant elastic modulus on the stress distribution around LTI carbon and aluminum oxide dental implants, J. Biomed. Mater. Res. 15 (1981) 879–887, https://doi.org/10.1002/jbm.820150612.

[13] T. Albrektsson, B. Chrcanovic, P.O. Östman, L. Sennerby, Initial and long-term crestal bone responses to modern dental implants, Periodontol 73 (2017) 41–50, https://doi.org/10.1111/prd.12176, 2000.

[14] H.D. Jung, T.S. Jang, L. Wang, H.E. Kim, Y.H. Koh, J. Song, Novel strategy for mechanically tunable and bioactive metal implants, Biomaterials 37 (2015) 49–61, https://doi.org/10.1016/j.biomaterials.2014.10.027.

[15] J. Ni, H. Ling, S. Zhang, Z. Wang, Z. Peng, C. Benyshek, R. Zan, A.K. Miri, Z. Li, X. Zhang, J. Lee, K.J. Lee, H.J. Kim, P. Tebon, T. Hoffman, M.R. Dokmeci, N. Ashammakhi, X. Li, A. Khademhosseini, Three-dimensional printing of metals for biomedical applications, Mater. Today Bio. 3 (2019) 100024, https://doi.org/10.1016/j.mtbio.2019.100024.

[16] S. Attarilar, F. Djavanroodi, M. Ebrahimi, K.J. Al-Fadhalah, L. Wang, M. Mozafari, Hierarchical microstructure tailoring of pure titanium for enhancing cellular response at tissue-implant interface, J. Biomed. Nanotechnol. 17 (2021) 115–130, https://doi.org/10.1166/jbn.2021.3015.

[17] D. Kuczyńska-Zemła, E. Kijeńska-Gawrońska, A. Chlanda, A. Sotniczuk, M. Pisarek, K. Topolski, W. Swieszkowski, H. Garbacz, Biological properties of a novel β-Ti alloy with a low young's modulus subjected to cold rolling, Appl. Surf. Sci. 511 (2020) 145523, https://doi.org/10.1016/j.apsusc.2020.145523.

[18] L. Wang, L. Xie, Y. Lv, L.-C. Zhang, L. Chen, Q. Meng, J. Qu, D. Zhang, W. Lu, Microstructure evolution and superelastic behavior in Ti-35Nb-2Ta-3Zr alloy processed by friction stir processing, Acta Mater. 131 (2017) 499–510, https://doi.org/10.1016/j.actamat.2017.03.079.

[19] L. Wang, Y. Wang, W. Huang, J. Liu, Y. Tang, L. Zhang, Y. Fu, L.-C. Zhang, W. Lu, Tensile and superelastic behaviors of Ti-35Nb-2Ta-3Zr with gradient structure, Mater. Des. 194 (2020) 108961, https://doi.org/10.1016/j.matdes.2020.108961.

[20] B.Q. Li, X.C. Li, X. Lu, Microstructure and compressive properties of porous Ti-Nb-Ta-Zr alloy for orthopedic applications, J. Mater. Res. 34 (2019) 4045–4055, https://doi.org/10.1557/jmr.2019.361.

[21] W. Zhou, M. Souissi, T. Abe, R. Sahara, P.H.L. Sit, K. Tsuchiya, Evaluating the phase stability of binary titanium alloy Ti-X (X = Mo, Nb, Al, and Zr) using first-principles calculations and a Debye model, Calphad 71 (2020) 102207, https://doi.org/10.1016/j.calphad.2020.102207.

[22] D. Kurniawan, F.M. Nor, H.Y. Lee, J.Y. Lim, Finite element analysis of bone–implant biomechanics: refinement through featuring various osseointegration conditions, Int. J. Oral Maxillofac. Surg. 41 (2012) 1090–1096, https://doi.org/10.1016/j.ijom.2011.12.026.

[23] P. Li, J. Long, W. Tang, J. Li, R. Liang, D.W. Tian, Stress distribution on the mandibular condyle and the distraction area in distraction osteogenesis by finite element analysis, J. Craniofac. Surg. 24 (2013) 1031–1037, https://doi.org/10.1097/SCS.0b013e31827ff348.

[24] L. Baggi, I. Cappelloni, M. Di Girolamo, F. Maceri, G. Vairo, The influence of implant diameter and length on stress distribution of osseointegrated implants related to crestal bone geometry: a three-dimensional finite element analysis, J. Prosthet. Dent 100 (2008) 422–431, https://doi.org/10.1016/s0022-3913(08)60259-0.

[25] M.T. Borges Radaelli, H.T. Idogava, A.O. Spazzin, P.Y. Noritomi, N. Boscato, Parafunctional loading and occlusal device on stress distribution around implants: a 3D finite element analysis, J. Prosthet. Dent 120 (2018) 565–572, https://doi.org/10.1016/j.prosdent.2017.12.023.

[26] J. Han, J. Hou, G. Zhou, C. Wang, Y. Fan, A histological and biomechanical study of bone stress and bone remodeling around immediately loaded implants, Sci. China Life Sci. 57 (2014) 618–626, https://doi.org/10.1007/s11427-014-4657-7.

[27] V. Demenko, I. Linetskiy, K. Nesvit, A. Shevchenko, Ultimate masticatory force as a criterion in implant selection, J. Dent. Res. 90 (2011) 1211–1215, https://doi.org/10.1177/0022034511417442.

[28] S. Shahriari, A. Parandakh, M.M. Khani, N. Azadikhah, P. Naraghi, M. Aeinevand, M. Nikkhoo, A. Khojasteh, The effect of mandibular flexure on stress distribution in the all-on-4 treated edentulous mandible: a comparative finite-element study based on mechanostat theory, J. Long Term Eff. Med. Implants 29 (2019) 79–86, https://doi.org/10.1615/JLongTermEffMedImplants.2019030866.

[29] G. Saravana Kumar, S.P. George, Optimization of custom cementless stem using finite element analysis and elastic modulus distribution for reducing stress-shielding effect, Proc. Inst. Mech. Eng. H 231 (2017) 149–159, https://doi.org/10.1177/0954411916686125.

[30] C. Schouten, G.J. Meijer, J.J. van den Beucken, P.H. Spauwen, J.A. Jansen, A novel implantation model for evaluation of bone healing response to dental implants: the goat iliac crest, Clin. Oral Implants Res. 21 (2010) 414–423, https://doi.org/10.1111/j.1600-0501.2009.01872.x.

[31] L. Podaropoulos, A.A. Veis, P. Trisi, S. Papadimitriou, C. Alexandridis, D. Kalyvas, Bone reactions around dental implants subjected to progressive static load: an experimental study in dogs, Clin. Oral Implants Res. 27 (2016) 910–917, https://doi.org/10.1111/clr.12658.

[32] J. Du, P. Xie, S. Lin, Y. Wu, D. Zeng, Y. Li, X. Jiang, Time-phase sequential utilization of adipose-derived mesenchymal stem cells on mesoporous bioactive glass for restoration of critical size bone defects, ACS Appl. Mater. Interfaces 10 (2018) 28340–28350, https://doi.org/10.1021/acsami.8b08563.

[33] Q. Wei, L. Wang, Y. Fu, J. Qin, W. Lu, D. Zhang, Influence of oxygen content on microstructure and mechanical properties of Ti–Nb–Ta–Zr alloy, Mater. Des. 32 (2011) 2934–2939, https://doi.org/10.1016/j.matdes.2010.11.049.

[34] J. Chen, F. Ma, P. Liu, C. Wang, X. Liu, W. Li, Q. Han, Effects of Nb on superelasticity and low modulus properties of metastable β-type Ti-Nb-Ta-Zr biomedical alloys, J. Mater. Eng. Perform. 28 (2019) 1410–1418, https://doi.org/10.1007/s11665-019-03897-4.

[35] T. Lee, M. Nakai, M. Niinomi, C.H. Park, C.S. Lee, Phase transformation and its effect on mechanical characteristics in warm-deformed Ti-29Nb-13Ta-4.6Zr alloy, Met. Mater. Int. 21 (2015) 202–207, https://doi.org/10.1007/s12540-015-1025-5.

[36] M. Niinomi, Y. Liu, M. Nakai, H. Liu, H. Li, Biomedical titanium alloys with Young's moduli close to that of cortical bone, Regen Biomater. 3 (2016) 173–185, https://doi.org/10.1093/rb/rbw016.

[37] M. Niinomi, T. Akahori, S. Katsura, K. Yamauchi, M. Ogawa, Mechanical characteristics and microstructure of drawn wire of Ti–29Nb–13Ta–4.6Zr for biomedical applications, Mater. Sci. Eng. C 27 (2007) 154–161, https://doi.org/10.1016/j.msec.2006.04.008.

[38] R. Ummethala, P.S. Karamched, S. Rathinavelu, N. Singh, A. Aggarwal, K. Sun, E. Ivanov, L. Kollo, I. Okulov, J. Eckert, K.G. Prashanth, Selective laser melting of high-strength, low-modulus Ti–35Nb–7Zr–5Ta alloy, Materialia 14 (2020), https://doi.org/10.1016/j.mtla.2020.100941.

[39] R. Banerjee, S. Nag, S. Samuel, H.L. Fraser, Laser-deposited Ti-Nb-Zr-Ta orthopedic alloys, J. Biomed. Mater. Res. 78 (2006) 298–305, https://doi.org/10.1002/jbm.a.30694.

[40] L.M. Elias, S.G. Schneider, S. Schneider, H.M. Silva, F. Malvisi, Microstructural and mechanical characterization of biomedical Ti–Nb–Zr(–Ta) alloys, Mater. Sci. Eng., A 432 (2006) 108–112, https://doi.org/10.1016/j.msea.2006.06.013.

[41] J.E. Bertram, S.M. Swartz, The 'law of bone transformation': a case of crying Wolff? Biol. Rev. Camb. Phil. Soc. 66 (1991) 245–273, https://doi.org/10.1111/j.1469-185x.1991.tb01142.x.

[42] T. Matsuzaki, Y. Ayukawa, Y. Matsushita, N. Sakai, M. Matsuzaki, T. Masuzaki, T. Haraguchi, Y. Ogino, K. Koyano, Effect of post-osseointegration loading magnitude on the dynamics of peri-implant bone: a finite element analysis and in vivo study, J. Prosthodont. Res. 63 (2019) 453–459, https://doi.org/10.1016/j.jpor.2018.10.009.

[43] L. Wang, X. You, S. Lotinun, L. Zhang, N. Wu, W. Zou, Mechanical sensing protein PIEZO1 regulates bone homeostasis via osteoblast-osteoclast crosstalk, Nat. Commun. 11 (2020) 282, https://doi.org/10.1038/s41467-019-14146-6.

[44] N.J. Hallab, C. Vermes, C. Messina, K.A. Roebuck, T.T. Glant, J.J. Jacobs, Concentration- and composition-dependent effects of metal ions on human MG-63 osteoblasts, J. Biomed. Mater. Res. 60 (2002) 420–433, https://doi.org/10.1002/jbm.10106.

[45] M. Geetha, A.K. Singh, R. Asokamani, A.K. Gogia, Ti based biomaterials, the ultimate choice for orthopaedic implants – a review, Prog. Mater. Sci. 54 (2009) 397–425, https://doi.org/10.1016/j.pmatsci.2008.06.004.

[46] M. Niinomi, M. Nakai, J. Hieda, Development of new metallic alloys for biomedical applications, Acta Biomater 8 (2012) 3888–3903, https://doi.org/10.1016/j.actbio.2012.06.037.

[47] N. Sakaguchi, M. Niinomi, T. Akahori, J. Takeda, H. Toda, Effect of Ta content on mechanical properties of Ti-30Nb-XTa-5Zr, Mater. Sci. Eng. C-Biomi. Supramol. Syst. 25 (2005) 370–376, https://doi.org/10.1016/j.msec.2005.04.003.

[48] L. Wang, J. Qu, L. Chen, Q. Meng, L.-C. Zhang, J. Qin, D. Zhang, W. Lu, Investigation of deformation mechanisms in β-type Ti-35Nb-2Ta-3Zr alloy via FSP leading to surface strengthening, Metall. Mater. Trans. 46 (2015) 4813–4818, https://doi.org/10.1007/s11661-015-3089-8.

[49] Y. Yang, P. Castany, E. Bertrand, M. Cornen, J.X. Lin, T. Gloriant, Stress release-induced interfacial twin boundary omega phase formation in it a beta type Ti-based single crystal displaying stress-induced alpha '' martensitic transformation, Acta Mater. 149 (2018) 97–107, https://doi.org/10.1016/j.actamat.2018.02.036.

[50] Q. Li, J.J. Li, G.H. Ma, X.Y. Liu, D. Pan, Influence of omega phase precipitation on mechanical performance and corrosion resistance of Ti-Nb-Zr alloy, Mater. Des. 111 (2016) 421–428, https://doi.org/10.1016/j.matdes.2016.09.026.

[51] Q. Liu, Q. Meng, S. Guo, X. Zhao, α′ Type Ti–Nb–Zr alloys with ultra-low Young's modulus and high strength, Prog. Nat. Sci.: Mater. Int. 23 (2013) 562–565, https://doi.org/10.1016/j.pnsc.2013.11.005.

[52] K. Bertl, M. Subotic, P. Heimel, U.Y. Schwarze, S. Tangl, C. Ulm, Morphometric characteristics of cortical and trabecular bone in atrophic edentulous mandibles, Clin. Oral Implants Res. 26 (2015) 780–787, https://doi.org/10.1111/clr.12340.

[53] A. Tabassum, G.J. Meijer, X.F. Walboomers, J.A. Jansen, Evaluation of primary and secondary stability of titanium implants using different surgical techniques, Clin. Oral Implants Res. 25 (2014) 487–492, https://doi.org/10.1111/clr.12180.

[54] J.L. Calvo Guirado, A.F. Lucero-Sanchez, A. Boquete Castro, M. Abboud, S. Gehrke, M. Fernandez Dominguez, R.A. Delgado Ruiz, Peri-implant behavior of sloped shoulder dental implants used for all-on-four protocols: an histomorphometric analysis in dogs, Materials 11 (2018) 119, https://doi.org/10.3390/ma11010119.

[55] T. Berglundh, I. Abrahamsson, N.P. Lang, J. Lindhe, De novo alveolar bone formation adjacent to endosseous implants, Clin. Oral Implants Res. 14 (2003) 251–262, https://doi.org/10.1034/j.1600-0501.2003.00972.x.

[56] A.F. Mavrogenis, R. Dimitriou, J. Parvizi, G.C. Babis, Biology of implant osseointegration, J. Musculoskelet. Neuronal Interact. 9 (2009) 61–71.

[57] M. Atsumi, S.H. Park, H.L. Wang, Methods used to assess implant stability: current status, Int. J. Oral Maxillofac. Implants 22 (2007) 743–754.

[58] J.B. Brunski, In Vivo bone response to biomechanical loading at the bone/dental-implant interface, Adv. Dent. Res. 13 (1999) 99–119, https://doi.org/10.1177/08959374990130012301.

[59] D. Lee, C. Park, Y. Lim, H. Cho, A metal artifact reduction method using a fully convolutional network in the sinogram and image domains for dental computed tomography, J. Digit. Imag. 33 (2020) 538–546, https://doi.org/10.1007/s10278-019-00297-x.

[60] R. Bernhardt, D. Scharnweber, B. Müller, P. Thurner, H. Schliephake, P. Wyss, F. Beckmann, J. Goebbels, H. Worch, Comparison of microfocus- and synchrotron X-ray tomography for the analysis of osteointegration around Ti6Al4V implants, Eur. Cell. Mater. 7 (2004) 42–51, https://doi.org/10.22203/ecm.v007a05, discussion 51.

[61] C. Schouten, G.J. Meijer, J.J. van den Beucken, P.H. Spauwen, J.A. Jansen, The quantitative assessment of peri-implant bone responses using histomorphometry and micro-computed tomography, Biomaterials 30 (2009) 4539–4549, https://doi.org/10.1016/j.biomaterials.2009.05.017.

[62] A. Naveau, K. Shinmyouzu, C. Moore, L. Avivi-Arber, J. Jokerst, S. Koka, Etiology and measurement of peri-implant crestal bone loss (CBL), J. Clin. Med. 8 (2019), https://doi.org/10.3390/jcm8020166.

[63] R.A. Delgado-Ruiz, J.L. Calvo-Guirado, G.E. Romanos, Effects of occlusal forces on the peri-implant-bone interface stability, Periodontol 81 (2019) 179–193, https://doi.org/10.1111/prd.12291, 2000.

[64] R.A. Delgado-Ruiz, J.L. Calvo-Guirado, M. Abboud, M.P. Ramirez-Fernandez, J.E. Mate-Sanchez de Val, B. Negri, D. Rothamel, Histologic and histomorphometric behavior of microgrooved zirconia dental implants with immediate loading, Clin. Implant Dent. Relat. Res. 16 (2014) 856–872, https://doi.org/10.1111/cid.12069.

[65] H.M. Frost, A 2003 update of bone physiology and Wolff's Law for clinicians, Angle Orthod 74 (2004) 3–15, https://doi.org/10.1043/0003-3219(2004)074<0003:AUOBPA>2.0.CO;2.

[66] P.J. Denard, P. Raiss, R. Gobezie, T.B. Edwards, E. Lederman, Stress shielding of the humerus in press-fit anatomic shoulder arthroplasty: review and recommendations for evaluation, J. Shoulder Elbow Surg. 27 (2018) 1139–1147, https://doi.org/10.1016/j.jse.2017.12.020.